Review of
Scientific Instruments

ARTICLE

pubs.aip.org/aip/rsi

Vacuum chamber for deposition of gradient thin films: Toward high-throughput structure–property correlative studies

Cite as: Rev. Sci. Instrum. 96, 053905 (2025); doi: 10.1063/5.0251290
Submitted: 1 December 2024 • Accepted: 15 April 2025 •
Published Online: 8 May 2025

View Online Export Citation CrossMark

Dmitry Lapkin,[a] Roody Nasro, Jakub Hagara, Bernd Hofferberth, Alexander Hinderhofer, Alexander Gerlach, and Frank Schreiber

AFFILIATIONS

University of Tübingen, Auf der Morgenstelle 10, 72076 Tübingen, Germany

[a] **Author to whom correspondence should be addressed:** dmitry.lapkin@uni-tuebingen.de

ABSTRACT

The advancement of materials science and application in complex multi-component systems is increasingly dependent on high-throughput studies that can efficiently explore the vast compositional space of materials. However, traditional sample preparation methods often struggle to keep pace with modern characterization techniques and data analysis capabilities. To address this challenge, we present a vacuum deposition chamber designed to produce gradient thin films. This chamber enables the deposition of single-component films with thickness gradients or multi-component films with continuous compositional gradients in a single experimental run. Our approach features a custom-designed moving shutter mechanism, which allows precise control over the deposition process and eliminates the need for multiple samples with discrete compositions. This significantly reduces research time and minimizes inconsistencies associated with the production of several individual samples. As a proof of concept, we deposited single-component gradient films of pentacene and diindenoperylene, which are widely studied in thin films for organic optoelectronic applications, and their corresponding binary gradient film. X-ray reflectivity measurements confirm the linear thickness gradients in the former and the linear compositional gradient in the latter samples.

I. INTRODUCTION

The technological progress of the recent decades would not have been possible without the development of new materials. Often, the materials with the optimal characteristics for applications are complex multi-component systems with rather nontrivial composition–property dependencies. The compositional optimization of new materials necessitates the high-throughput screening of a multitude of compositions, which must be investigated to elucidate the non-linear and non-monotonic dependencies.[1] In this regard, data-driven material science has the potential to revolutionize materials discovery and development by efficiently exploring vast material spaces and providing insights that may not be apparent through traditional methods. It enables researchers to accelerate the identification of new materials with desired properties for specific applications. Such high-throughput data-driven studies comprise two key elements: the combinatorial preparation of suitable sample libraries spanning wide compositional ranges and the high-throughput screening of the structure and properties of the synthesized samples.[2–4]

The first approaches to data-driven material screening were proposed over half a century ago,[5,6] but neither received the deserved attention nor development at that time due to the lack of suitable fast sample investigation methods and data analysis techniques. Over the past few decades, there have been significant advances in the spatial resolution and throughput of various experimental methods, which have led to a renaissance of these ideas. For instance, x-ray scattering methods are widely used in modern material science for structural investigations due to their large penetration depth, high spatial resolution, and wide range of probed length scales.[7] Grazing-incidence techniques, such as grazing-incidence small- and wide-angle x-ray scattering (GISAXS/GIWAXS), are particularly useful for structural studies of thin films.[8,9] Modern x-ray optics enable the tight x-ray beam focusing down to submicrometer sizes, thereby providing excellent spatial resolution, which is highly beneficial for spatially resolved investigations of the sample libraries.

The enormous brilliance of modern x-ray sources, such as diffraction-limited synchrotron sources,[10,11] significantly reduces measurement times without compromising resolution. Complementing these experimental advancements, machine learning (ML) based techniques have emerged to support rapid data analysis across a variety of experimental methods,[12,13] including x-ray scattering.[14,15] The software developed for the analysis of grazing-incidence scattering data and x-ray reflectometry provides almost instantaneous on-the-fly processing of the measured data.[16–20] Thus, the combination of fast sample screening methods with ML-based data analysis provides a basis for high-throughput studies calling for suitable sample preparation techniques.

Since the pioneering studies, numerous techniques have been developed to prepare multiple samples on a single substrate, simplifying screening and alignment processes. Such sample libraries can be discrete, consisting of multiple separated samples/sample regions with uniform compositions, or gradient, with continuously changing composition/preparation conditions across the sample.[3] Discrete samples are preferable when a physical isolation of the samples is required, for example, for electrophysical characterization.[21,22] Such isolation can be easily achieved using solvent-based sample preparation methods, such as spin-coating, drop-casting, or ink-jet printing.[22–24] On the other hand, solvent-free methods such as physical or chemical vapor deposition (PVD/CVD) are more suitable for the deposition of gradient samples. These samples can also be easily converted into discrete sample libraries by using a shadow mask for separating different regions. The gradient approach allows quasi-continuous probing of the structure and properties of a material as a function of its composition, with the spatial (i.e., compositional) resolution defined by the probe size. Although the compositional resolution is still limited to the gradient slope within the probe size, with the available spatial resolution of the modern techniques it is still superior in comparison with the compositional/conditional variability during consequent sample preparation. In the case of PVD, which we mostly focus on, three main approaches have been developed.

The first one comprises an off-axis deposition using multiple sources with partially overlapping material beams.[5,25–27] This approach does not require any moving parts in the evacuated deposition chamber and allows easy combination of several components. At the same time, the samples prepared this way have a limited compositional range, and potentially inhomogeneous thickness and unclear composition distribution defined by the exact material beam profiles. Consequently, it requires either complicated simulations[25,26] or additional analysis by x-ray photoelectron spectroscopy (XPS) or energy-dispersive x-ray spectroscopy (EDX)[25,27] to reconstruct the thickness and composition distribution within the sample.

Another approach makes use of extended material sources with fixed shadow masks, producing almost perfect linear gradients.[28,29] However, this method requires elongated and uniform sources, i.e., vast amounts of material, which is quite challenging in the case of complex chemical synthesis of the material.

The approach with moving shadow masks allows a high degree of control over the direction and the span of the composition gradient.[7,30–37] Typically, the approach involves a single shadow mask located in close proximity to the substrate surface and moving linearly during deposition from a single material source. The second and subsequent materials are deposited sequentially during the next cycles of shadow mask movement. One of the limitations of this method is that the components cannot be co-deposited simultaneously, instead forming wedges of different materials. Annealing of the samples is then required to facilitate vertical interdiffusion of the materials. However, annealing may not always be possible or could result in incomplete mixing unless each wedge is thinner than a single monolayer. The latter requirement is easily met for organic molecular deposition due to the low deposition rate and relatively large unit cell dimensions. Hence, in this case, the period of the shutter movement can be set much shorter than the time required for the deposition of a single molecular layer.

In this work, we present an approach for the deposition of multi-component molecular thin films with compositional gradients in single runs, utilizing a specially developed vacuum deposition chamber. The developed moving shutter system with two shutter blades allows simultaneous co-deposition of different materials, resulting in their immediate mixing without the need for subsequent annealing. Moreover, the developed approach allows for the simultaneous probing of different compositions without requiring multiple sample preparations, thereby avoiding the potential for unintentional variations in sample preparation conditions. The combination of a well-defined gradient composition and the high spatial resolution of modern material investigation methods shown in Fig. 1 makes such samples ideal candidates for high-throughput compositionally resolved studies of structure–property correlations in thin films.

While the focus of this work is on binary systems, the chamber can of course also be used for single-component samples with a lateral gradient in thickness, which is also extremely useful for many

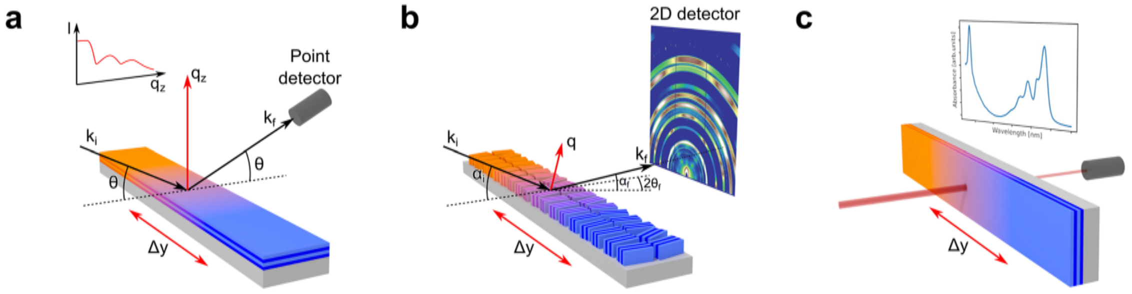

FIG. 1. Possible techniques to access the structural and electronic properties of the gradient thin films: (a) specular x-ray reflectivity (XRR), (b) grazing-incidence wide-angle x-ray scattering (GIWAXS), and (c) absorption spectroscopy in the UV–vis range.

thickness-dependent phenomena.[21] To some extent, such samples can also substitute *in situ* studies of film growth. However, it should be noted that the growth processes are highly complex and in non-equilibrium, and many features can only be observed in real time during the growth.[38–41]

II. CHAMBER DESIGN

A. Overall layout

A photo of the chamber is shown in Fig. 2(a). The chamber consists of a main spherical evaporation chamber and a cylindrical load-lock chamber connected with a sliding UHV gate valve. The sample can be transferred between the chambers by using a transfer rod and is mounted in the main chamber on a four-axis manipulator allowing alignment of the sample in respect to the evaporated material beams. The bottom part of the main chamber represents the core component of the developed design: the evaporation block with a moving shutter shown in Fig. 2(b) and described in detail below. All the components are mounted on standard ConFlat (CF) flanges of different sizes.

Both main and load-lock chambers are equipped with viewports, which allow real-time observation of the sample inside, the moving shutter and the crucible outlets. Improved visibility during operation can be achieved by using an external light source.

B. Vacuum system

Both main and load-lock chambers are equipped with separate Pfeiffer Balzers TPU 170 turbo molecular pumps coupled to roughening pumps. The main chamber is additionally fitted by a Riber ion getter and a titanium sublimation pump. The pressure is monitored by separate cold cathode Pfeiffer Balzers ion gauges in both chambers. This makes the chamber UHV-compatible. At the present commissioning stage, when the chamber is frequently vented and exposed to air and moisture, the base pressure reaches 10^{-8} mbar but can be significantly improved by a bakeout.

To ensure that the vacuum is preserved in case of a power outage, both chambers are equipped with gate valves between the chambers and the turbo pumps. The main chamber valve is pneumatically actuated; hence, it automatically closes in the absence of electrical power. This feature enhances the reliability of the system and maintains vacuum conditions even in unexpected situations.

C. Evaporation block

The main feature of the chamber is an evaporation block mounted on a custom-made CF200 cluster flange on the bottom of the main chamber depicted in Fig. 2(b). The cluster flange, manufactured by VACOM Vakuum Komponenten & Messtechnik GmbH, has four CF40 flanges arranged symmetrically around its center. Each of the flanges is tilted inward, focusing the outlets toward the same point at the center of the spherical main chamber. Two of the flanges are currently equipped with low-temperature effusion cells (OLED-40-2-WK-SHM, CreaTec Fischer & Co. GmbH), allowing deposition of single-component and binary blend films. Each cell utilizes a K-type thermocouple, connected to Eurotherm 3508 PID (Proportional-Integral-Derivative) controllers for precise temperature regulation. The effusion cells are suitable for the evaporation of organic materials, such as small molecule organic semiconductors (OSC), but they can be replaced by other effusion cells expanding the application area to almost any material class. The evaporation block can be further upgraded with a third effusion cell that would enable high-throughput studies of ternary blends.

The uniformity of the material beam at the sample position is crucial for creating the expected linear compositional gradient. The main factors affecting the material beam profile are the opening angle of the crucibles used and the distance between the crucible and the sample position.[42] The latter is defined by the UHV chamber geometry, so we optimized the crucible geometry to achieve uniform material distribution on the length scale of 50 mm (the standard sample size, see Sec. II D for details). At present, we use custom-made aluminum oxide crucibles with 5 mm diameter (maximum possible diameter for the used effusion cells) and 15 mm depth

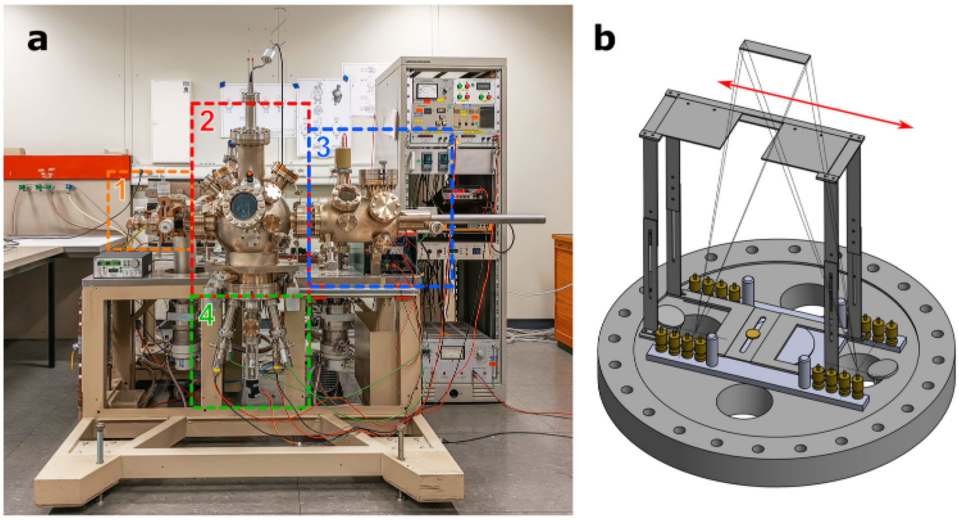

FIG. 2. (a) Photo of the developed OMBD chamber with main components highlighted with colored boxes: 1—sample holder manipulator, 2—main deposition chamber, 3—load-lock chamber, and 4—evaporation block with moving shutter driven by a stepper motor. (b) Sketch of the evaporation block with two effusion cells mounted on the bottom plate and a moving shutter composed of two blades. The red arrows show the direction of the shutter blades movement.

that give an opening angle of about 30° depending on the filling level. This opening angle provides an almost uniform material beam profile with 3% thickness deviation at the sample position (about 300 mm upstream from the crucible opening), see supplementary material, Fig. S1 for details.

The deposition rates are monitored *in situ* using a quartz crystal microbalance (QCM) from INFICON (gold coated crystal, 6 MHz nominal frequency), which is placed in close proximity to the sample for accurate and real-time thickness determination. The crystal is connected to an INFICON OSC-100B oscillator and controlled with an INFICON SQM-160 digital controller. The QCM readings for each material are calibrated to the real deposited thickness with XRR measurements of the corresponding single-component pure material films.

The desired gradient distribution of the components is ensured by a specially designed moving shutter**,** which consists of two connected steel blades moving synchronously along the gradient axis back and forth. The blades are mounted on a steel frame shown in Fig. 2(b), which allows calibration of the height and distance between the blades. The bottom base of the frame is supported by brass rollers that allow uniaxial translation movement of the whole shutter. The shutter is brought into motion by a Scotch yoke (slotted link mechanism). The rotating part of the Scotch yoke is driven by a stepper motor with 200 steps per rotation (ST4118D1804-B, Nanotec Electronic GmbH & Co). The latter is located on the axis outside the evacuated volume. The torque is transmitted into the chamber by a barrel-based rotary feedthrough. This design is simple to implement and highly reliable as it does not require the placement of motors/drives within the evacuated UHV volume or using translational feedthroughs. The motor is coupled with an MAKERFACTORY MF-6402405 stepper motor driver module and controlled by an Espressif ESP32-WROVER-E microcontroller that uses a custom software written in Arduino IDE. This ensures precise control of the shutter movement.

To maintain the constant linear speed of the shutter required for linear compositional/thickness gradient, the step delay τ of the stepper motor as function of the angular position φ is calculated as

$$\tau = \frac{T}{4}|\sin\,\varphi|\,\mathrm{d}\varphi, \tag{1}$$

where $t = 0$ corresponds to the extreme position of the shutter ($\varphi = 0°$ or $180°$), T is the desired period of the movement, and $\mathrm{d}\varphi = 2\pi/200$ is the angular step in radians. A period of $T = 1$ min provides a sufficient degree of intra-layer component intermixing at the used evaporation rates of about 2 Å/min and can be easily maintained by the currently used stepper motor controller, which adjusts the step delay according to Eq. (1).

D. Sample handling

The sample holder is designed to accommodate two substrates with the size of 52×10 mm^2 next to each other with their long dimension (y axis) along the gradient (shutter movement) axis, as shown in Fig. 3. The sample holder is made of steel and has four polytetrafluoroethylene clamps to hold the substrates. It also has a cross-shaped pin on one of the short sides to mount it in a corresponding socket on the end of a transfer rod, as shown in Fig. 3. The sample holder is fixed inside the socket in the vertical position and is expelled out of the socket by a spring on the pin tail in the horizontal position. The transfer rod has a single translation with a large range, which allows transferring the samples from the loading window in the load-lock to the sample stage at the center of the main chamber.

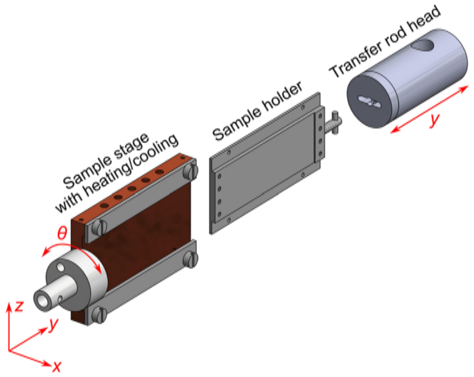

FIG. 3. Sketch of the sample handling system. The sample stage comprises a copper block with steel rails and is mounted on a manipulator with three translational and one rotational degree of freedom. The steel sample holder has counter-rails to fit into the sample stage, a cross pin to fit into the transfer rod, and clamps to mount the substrates (not shown in the figure). The transfer rod head has a socket for the cross pin and is mounted on a transfer rod with one translational axis.

The sample stage is mounted on a manipulator with three translational (x, y, and z) and one rotational (θ) degrees of freedom, shown in Fig. 3, allowing sample holder transfer from the transfer rod and precise positioning of the sample with respect to the material beams. The sample stage consists of a massive copper block with two steel rails on opposite edges of one of the block sides. The sample holder can freely slide between the copper block and the rails in the horizontal direction. By rotating the sample stage after inserting the sample holder, one can take it out of the transfer rod and retract the transfer rod back into the load-lock chamber. The sample stage is then brought by the manipulator to a calibrated position in the area inside the chamber, where the material beams cross.

The copper block on the sample stage can be heated by a resistive heating coil and cooled down by liquid nitrogen vapor, whereby K-type thermocouples attached to the block enable temperature monitoring. The tight thermal contact between the copper block and the sample holder is provided by the spring-loaded rails on the sample stage described above. This provides the possibility to control the substrate temperature during the growth, which affects the structure and morphology of many types of thin film materials. In addition, this offers the option to anneal the substrate before the deposition or the sample after the deposition.

III. RESULTS AND DISCUSSION

A. Thickness vs composition gradient

The linear movement of the shutter blades results in a linear material amount gradient, as will be confirmed in Sec. III B for single-component films. In the case of mixed multi-component films, most material properties depend not on the specific volume ratio of components, but on their molar ratio. Given the linear amount distribution of the components, one can easily calculate the molar fractions of the components as a function of the position on the sample. Let the partial thicknesses of the components A and B be described as

$$h_A = A\frac{l-y}{l}, \qquad h_B = B\frac{y}{l}, \tag{2}$$

where A and B represent the maximum thicknesses of the components A and B, respectively, y is the coordinate along the gradient axis, and l is the length of the gradient region, as shown in Fig. 4(a). Then, the molar fraction of the components A and B with the molar masses μ_A and μ_B, and densities ρ_A and ρ_B, respectively, can be expressed as

$$x_A = \frac{(l-y)}{\chi y + (l-y)}, \qquad x_B = \frac{\chi y}{\chi y + (l-y)}, \tag{3}$$

where $\chi = B\mu_B\rho_A \big/ A\mu_A\rho_B$. For $\chi = 1$, it results in linear dependencies along the gradient axis, while for $\chi \neq 1$, it deviates from the linear behavior, as shown in Fig. 4(b). Nevertheless, Eq. (3) allows the calculation of the actual molar fractions for any value of χ (e.g., any nominal thicknesses A and B, and any material with arbitrary molar masses and densities). For example, for mixed PEN:DIP films (which we use as an application example; see details in the following) with equal nominal thicknesses $A = B$, the coefficient χ is 1.47. This makes it possible to study the structure and properties of the gradient films as a function of the molar fraction.

The sample stage and the moving shutter blade positions in our chamber are aligned in such a way that the resulting film has 2 mm of constant thickness of single components on each of the edges and 48 mm of a linear gradient between them. It allows us to study the full range of compositions ranging from one pure component to another.

B. Application example

We selected two widely studied OSC molecules, namely, pentacene (PEN) and diindenoperylene (DIP) as model materials due to the abundance of reference data.[38,43–45] With this application example, we aim to validate the linear thickness and gradient distribution capability of our design. We deposited separate PEN and DIP single-component films with thickness gradients and a binary PEN:DIP film with compositional gradient. Both materials were deposited at a rate of about 2 Å/min for 100 min in each case. The films were deposited simultaneously on silicon and quartz substrates kept at room temperature. The resulting thin films were studied by means of XRR to confirm the linear gradient distributions.

The samples were characterized with a General Electric XRD 3003-TT diffractometer equipped with a Cu-K$_{\alpha 1}$ X-ray source. The beam size was defined by a set of vertical slits to ~1 mm (FWHM). We scanned the sample along the gradient axis, measuring an XRR curve every 1 mm. Figures 5(a)–5(c) shows the resulting XRR curves for different spatial positions for all samples. At low q-values, one can see the Kiessig oscillations, which can be used to extract the film thickness h, roughness σ, and scattering length density (SLD) ρ. The Kiessig oscillations were fitted using a slab model with a single layer on a Si substrate, employing the *refnx* package.[46] We extracted the film parameters for each spatial position separately. Exemplary fits of the experimental curves are shown in the supplementary material, Figs. S2–S4.

The resulting thicknesses and SLDs of the single-component films as functions of the spatial positions are shown in the supplementary material, Figs. S2 and S3. Due to the layered structure of crystalline organic thin films, thickness is not continuous and the SLD reflects the layer coverages. However, on their own, they are not a sufficient measure of the deposited material. Hence, the most adequate value reflecting the actual amount of the deposited material is the product ρh of the extracted thickness and SLD shown in Fig. 5(d).

One can see an almost perfect linear dependency of the amount of material on the lateral coordinate, confirming the reliability of the proposed concept. The slight deviation from linearity is due to

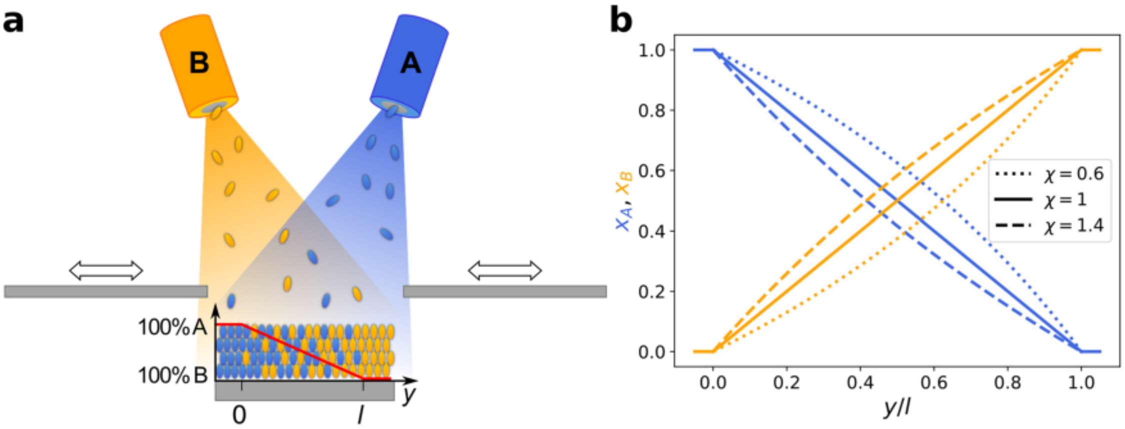

FIG. 4. (a) Schematic of the deposition process. Two molecular beams are interrupted by the shutter moving back-and-forth with constant speed. The resulting film has a compositional gradient along the y axis in the range from 0 to l. (b) Deviation of the molar fractions from the linear dependencies for different values of the gradient parameter χ defined in Eq. (3).

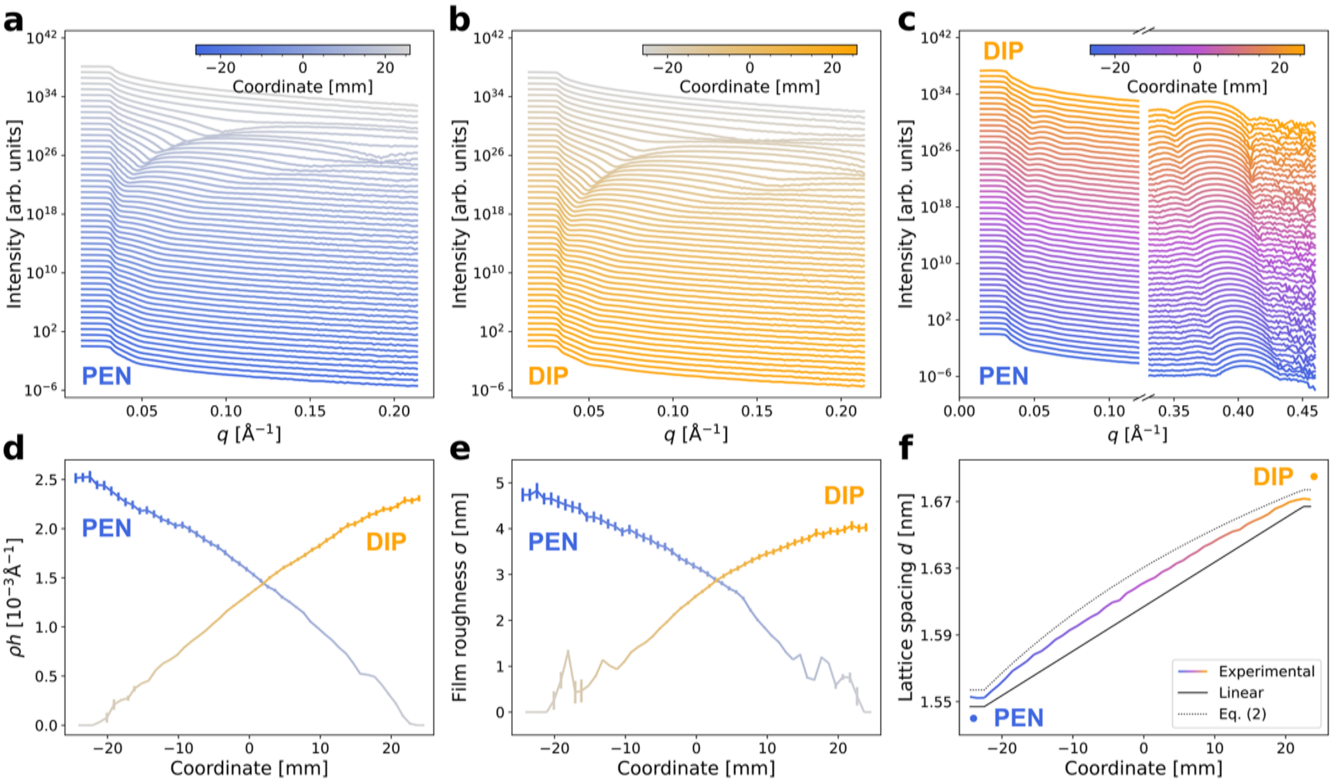

FIG. 5. (a)–(c) XRR curves from PEN (a) and DIP (b) single-component films with a thickness gradient, and a PEN:DIP (c) film with the compositional gradient measured at different spatial points along the gradient axis. The curves are shifted vertically for better visibility. (d) and (e) Extracted dependencies of the product of (d) the scattered length density ρ and film thickness h, and (e) the film roughness σ for the single-component thin films as functions of the coordinate. (f) Extracted dependency of the out-of-plane lattice spacing d for the gradient PEN:DIP film on the coordinate along the gradient axis (gradient solid line). The solid circles show the values for thin-film phases of pure PEN and DIP, respectively. The theoretical unit cell dependence according to Vegard's law with a molar fraction dependency: linear (black solid line) and according to Eq. (3) (black dotted line). The lines are shifted vertically for visibility.

imperfect uniform flux distribution in the material beams, defined by the crucible opening angle and finite cell-to-substrate distance, as was shown for uniform films. The thickness dependence of the mixed PEN:DIP film shown in the supplementary material, Fig. S4, also demonstrates a slightly non-linear profile with a root mean square deviation of 6% from a linear dependency.

The lateral (i.e., thickness) dependence of the roughness for single-component gradient films shown in Fig. 5(e) provides insights into the thin film growth modes.[47] In the thin regions of the films, the roughness is highly non-monotonous, which is characteristic for layer-by-layer growth. With increasing thickness, a transition to the square-root dependence characteristic for statistical growth is observed. This behavior aligns with previous studies on PEN and DIP thin films grown at room temperature.[48,49] The roughness of the mixed gradient film is also non-monotonous, as shown in the supplementary material, Fig. S4, and is in general lower for the mixed region than for pure components on the edges. This behavior is well known for mixed films forming solid solutions, including the PEN:DIP system,[50] but its discussion is beyond the scope of this paper.

We further analyzed the mixed film by measuring the q-range from 0.33 to 0.47 Å^{-1}, which contains the first out-of-plane Bragg peak corresponding to the out-of-plane lattice spacing (d_{PEN} = 15.4 Å and d_{DIP} = 16.8 Å for pure PEN[48] and DIP,[49] respectively). The Bragg peak was fitted by a Gaussian function and the extracted peak position q_0 was converted into the intra-layer distance $d = 2\pi/q_0$. The dependence of the lattice spacing d for the mixed PEN:DIP thin film on the coordinate is shown in Fig. 5(f). The measured values on the sample edges are slightly higher (lower) than those expected for pure PEN (DIP). We assume that the main reason is the wide beam available at our lab diffractometer, leading to averaging also over the mixed regions next to the sample edges. Between the edges, the intra-layer distance changes almost linearly with slight deviation toward higher values. This deviation was observed for several systems of molecules with different sizes forming solid solutions[44,51] and is caused by the fact that smaller molecules dissolve more easily in the crystal lattice of bigger molecules (PEN in DIP in this case). On the other hand, the dependence of the unit cell parameters on the molar fraction for solid solutions follows Vegard's law.[52] The theoretical prediction based on Vegard's law with the molar fraction dependence given by Eq. (3) aligns closer to the experimental data compared to a simple linear dependence, as shown in Fig. 5(f).

IV. CONCLUSIONS AND OUTLOOK

The developed chamber allows deposition of thin films with a thickness or compositional gradient. The moving shutter mechanism allows precise control over the component distribution, resulting in an almost perfect linear slope of the material amount along the sample axis. The molar ratio of the components can be easily calculated for each spatial point along the gradient axis given the material amounts on the edges. The robustness and durability of the system has been proven by the successful deposition of several dozen samples, demonstrating its reliability for high-throughput studies. The chamber represents a significant advancement in the field of high-throughput material research and opens up new possibilities for high-throughput, compositionally resolved studies of structure–property correlations in thin films. The planned upgrade of the developed chamber for ternary mixtures and other material classes opens up further perspectives in high-throughput material science. The vast amount of x-ray scattering data generated from such samples can be subjected to analysis by emerging ML-based approaches thus accelerating compositional optimization for applications.[4,15,19,20]

SUPPLEMENTARY MATERIAL

The supplementary material for this paper provides the specular x-ray reflectivity (XRR) data and analysis results, confirming (1) the uniform material distribution at the sample position using a single effusion cell with a stationary shutter, (2) a linear thickness gradient from a single effusion cell with a moving shutter, and (3) a linear binary compositional gradient from two effusion cells with a moving shutter.

ACKNOWLEDGMENTS

The project is partially funded by the German Research Foundation (DFG), by the Federal Ministry of Education and Research (BMBF), and the Baden-Württemberg Ministry of Science as part of the Excellence Strategy of the German Federal and State Governments. The authors acknowledge the Center for Light-Matter Interaction, Sensors & Analytics (LISA+) at the University of Tübingen for their support.

AUTHOR DECLARATIONS

Conflict of Interest

The authors have no conflicts to disclose.

Author Contributions

Dmitry Lapkin: Data curation (lead); Investigation (equal); Methodology (equal); Validation (equal); Visualization (lead); Writing – original draft (equal); Writing – review & editing (equal). **Roody Nasro**: Data curation (equal); Investigation (equal); Validation (equal); Visualization (supporting); Writing – original draft (supporting); Writing – review & editing (equal). **Jakub Hagara**: Methodology (equal); Resources (equal); Writing – review & editing (equal). **Bernd Hofferberth**: Methodology (equal); Resources (equal); Writing – review & editing (equal). **Alexander Hinderhofer**: Conceptualization (equal); Writing – review & editing (equal). **Alexander Gerlach**: Conceptualization (equal); Writing – original draft (supporting); Writing – review & editing (equal). **Frank Schreiber**: Conceptualization (equal); Project administration (equal); Supervision (equal); Writing – original draft (equal); Writing – review & editing (equal).

DATA AVAILABILITY

The data that support the findings of this study are available from the corresponding author upon reasonable request.

REFERENCES

[1] A. Ludwig, "Discovery of new materials using combinatorial synthesis and high-throughput characterization of thin-film materials libraries combined with computational methods," npj Comput. Mater. **5**, 70 (2019).

[2] R. Potyrailo and E. Amis, *High-Throughput Analysis: A Tool for Combinatorial Materials Science* (Springer US, 2012).

[3] P. J. McGinn, "Thin-film processing routes for combinatorial materials investigations—A review," ACS Comb. Sci. **21**, 501 (2019).

[4] J. M. Gregoire, L. Zhou, and J. A. Haber, "Combinatorial synthesis for AI-driven materials discovery," Nat. Synth. **2**, 493 (2023).

[5] K. Kennedy, T. Stefansky, G. Davy, V. F. Zackay, and E. R. Parker, "Rapid method for determining ternary-alloy phase diagrams," J. Appl. Phys. **36**, 3808 (1965).

[6] J. J. Hanak, "The 'multiple-sample concept' in materials research: Synthesis, compositional analysis and testing of entire multicomponent systems," J. Mater. Sci. **5**, 964 (1970).

[7] D. A. Kukuruznyak, H. Reichert, J. Okasinski, H. Dosch, T. Chikyow, J. Daniels, and V. Honkimäki, "High-throughput screening of combinatorial materials libraries by high-energy x-ray diffraction," Appl. Phys. Lett. **91**, 071916 (2007).

[8] U. Pietsch, V. Holy, and T. Baumbach, *High-resolution X-Ray Scattering: From Thin Films to Lateral Nanostructures* (Springer Science & Business Media, 2004).

[9] J. A. Steele, E. Solano, D. Hardy, D. Dayton, D. Ladd, K. White, P. Chen, J. Hou, H. Huang, R. A. Saha *et al.*, "How to GIWAXS: Grazing incidence wide angle X-ray scattering applied to metal halide perovskite thin films," Adv. Energy Mater. **13**, 2300760 (2023).

[10] P. Raimondi, "ESRF-EBS: The extremely brilliant source project," Synchrotron Radiat. News **29**, 8 (2016).

[11] C. G. Schroer, I. Agapov, W. Brefeld, R. Brinkmann, Y.-C. Chae, H.-C. Chao, M. Eriksson, J. Keil, X. Nuel Gavaldà, R. Röhlsberger, O. H. Seeck, M. Sprung, M. Tischer, R. Wanzenberg, and E. Weckert, "PETRA IV: The ultralow-emittance source project at DESY," J. Synchrotron Radiat. **25**, 1277 (2018).

[12] T. Mueller, A. G. Kusne, and R. Ramprasad, "Machine learning in materials science: Recent progress and emerging applications," Rev. Comput. Chem. **29**, 186 (2016).

[13] J. Wei, X. Chu, X.-Y. Sun, K. Xu, H.-X. Deng, J. Chen, Z. Wei, and M. Lei, "Machine learning in materials science," InfoMat **1**, 338 (2019).

[14] Z. Chen, N. Andrejevic, N. C. Drucker, T. Nguyen, R. P. Xian, T. Smidt, Y. Wang, R. Ernstorfer, D. A. Tennant, M. Chan, and M. Li, "Machine learning on neutron and X-ray scattering and spectroscopies," Chem. Phys. Rev. **2**, 031301 (2021).

[15] A. Hinderhofer, A. Greco, V. Starostin, V. Munteanu, L. Pithan, A. Gerlach, and F. Schreiber, "Machine learning for scattering data: Strategies, perspectives and applications to surface scattering," J. Appl. Crystallogr. **56**, 3 (2023).

[16] A. Greco, V. Starostin, C. Karapanagiotis, A. Hinderhofer, A. Gerlach, L. Pithan, S. Liehr, F. Schreiber, and S. Kowarik, "Fast fitting of reflectivity data of growing thin films using neural networks," J. Appl. Crystallogr. **52**, 1342 (2019).

[17] A. Greco, V. Starostin, A. Hinderhofer, A. Gerlach, M. W. A. Skoda, S. Kowarik, and F. Schreiber, "Neural network analysis of neutron and X-ray reflectivity data:

Pathological cases, performance and perspectives," Mach. Learn.: Sci. Technol. **2**, 045003 (2021).

[18] V. Starostin, V. Munteanu, A. Greco, E. Kneschaurek, A. Pleli, F. Bertram, A. Gerlach, A. Hinderhofer, and F. Schreiber, "Tracking perovskite crystallization via deep learning-based feature detection on 2D X-ray scattering data," npj Comput. Mater. **8**, 101 (2022).

[19] V. Starostin, L. Pithan, A. Greco, V. Munteanu, A. Gerlach, A. Hinderhofer, and F. Schreiber, "End-to-end deep learning pipeline for real-time processing of surface scattering data at synchrotron facilities," Synchrotron Radiat. News **35**, 21 (2022).

[20] V. Munteanu, V. Starostin, A. Greco, L. Pithan, A. Gerlach, A. Hinderhofer, S. Kowarik, and F. Schreiber, "Neural network analysis of neutron and X-ray reflectivity data incorporating prior knowledge," J. Appl. Crystallogr. **57**, 456 (2024).

[21] C. Schmitz, M. Thelakkat, and H.-W. Schmidt, "A combinatorial study of the dependence of organic LED characteristics on layer thickness," Adv. Mater. **11**, 821 (1999).

[22] J. Alstrup, M. Jørgensen, A. J. Medford, and F. C. Krebs, "Ultra fast and parsimonious materials screening for polymer solar cells using differentially pumped slot-die coating," ACS Appl. Mater. Interfaces **2**, 2819 (2010).

[23] A. Teichler, R. Eckardt, S. Hoeppener, C. Friebe, J. Perelaer, A. Senes, M. Morana, C. J. Brabec, and U. S. Schubert, "Combinatorial screening of polymer:Fullerene blends for organic solar cells by inkjet printing," Adv. Energy Mater. **1**, 105 (2011).

[24] M. Zeng, Y. Du, Q. Jiang, N. Kempf, C. Wei, M. V. Bimrose, A. N. M. Tanvir, H. Xu, J. Chen, D. J. Kirsch *et al.*, "High-throughput printing of combinatorial materials from aerosols," Nature **617**, 292 (2023).

[25] N. D. Bassim, P. K. Schenck, M. Otani, and H. Oguchi, "Model, prediction, and experimental verification of composition and thickness in continuous spread thin film combinatorial libraries grown by pulsed laser deposition," Rev. Sci. Instrum. **78**, 072203 (2007).

[26] S. O. Klemm, A. G. Martin, J. Lengsfeld, J.-C. Schauer, B. Schuhmacher, and A. W. Hassel, "Theoretical simulation and preparation of binary and ternary combinatorial libraries by thermal PVD," Phys. Status Solidi A **207**, 801 (2010).

[27] D. Priyadarshini, P. Kondratyuk, J. B. Miller, and A. J. Gellman, "Compact tool for deposition of composition spread alloy films," J. Vac. Sci. Technol., A **30**, 011503 (2012).

[28] S. Guerin and B. E. Hayden, "Physical vapor deposition method for the high-throughput synthesis of solid-state material libraries," J. Comb. Chem. **8**, 66 (2006).

[29] M. S. B. Darby, D. V. Karpinsky, J. Pokorny, S. Guerin, A. L. Kholkin, S. Miao, B. E. Hayden, and I. M. Reaney, "Synthesis and characterization of $Bi_{1-x}Nd_xFeO_3$ thin films deposited using a high throughput physical vapour deposition technique," Thin Solid Films **531**, 56 (2013).

[30] F. Tsui and L. He, "Techniques for combinatorial molecular beam epitaxy," Rev. Sci. Instrum. **76**, 062206 (2005).

[31] R. Takahashi, H. Kubota, M. Murakami, Y. Yamamoto, Y. Matsumoto, and H. Koinuma, "Design of combinatorial shadow masks for complete ternary-phase diagramming of solid state materials," J. Comb. Chem. **6**, 50 (2004).

[32] A. Ludwig, R. Zarnetta, S. Hamann, A. Savan, and S. Thienhaus, "Development of multifunctional thin films using high-throughput experimentation methods," Int. J. Mater. Res. **99**, 1144 (2008).

[33] C. Neuber, M. Bäte, M. Thelakkat, H.-W. Schmidt, H. Hänsel, H. Zettl, and G. Krausch, "Combinatorial preparation and characterization of thin-film multilayer electro-optical devices," Rev. Sci. Instrum. **78**, 072216 (2007).

[34] P. Ahmet, Y.-Z. Yoo, K. Hasegawa, H. Koinuma, and T. Chikyow, "Fabrication of three-component composition spread thin film with controlled composition and thickness," Appl. Phys. A **79**, 837 (2004).

[35] B. Fleutot, J. B. Miller, and A. J. Gellman, "Apparatus for deposition of composition spread alloy films: The rotatable shadow mask," J. Vac. Sci. Technol., A **30**, 061511 (2012).

[36] A. Janghorban, J. Pfetzing-Micklich, J. Frenzel, and A. Ludwig, "Investigation of the thin-film phase diagram of the Cr–Ni–Re system by high-throughput experimentation," Adv. Eng. Mater. **16**, 588 (2014).

[37] K. Kawashima, Y. Okamoto, O. Annayev, N. Toyokura, R. Takahashi, M. Lippmaa, K. Itaka, Y. Suzuki, N. Matsuki, and H. Koinuma, "Combinatorial screening of halide perovskite thin films and solar cells by mask-defined IR laser molecular beam epitaxy," Sci. Technol. Adv. Mater. **18**, 307 (2017).

[38] S. Kowarik, A. Gerlach, S. Sellner, F. Schreiber, L. Cavalcanti, and O. Konovalov, "Real-time observation of structural and orientational transitions during growth of organic thin films," Phys. Rev. Lett. **96**, 125504 (2006).

[39] K. A. Ritley, B. Krause, F. Schreiber, and H. Dosch, "A portable ultrahigh vacuum organic molecular beam deposition system for *in situ* x-ray diffraction measurements," Rev. Sci. Instrum. **72**, 1453 (2001).

[40] E. Annese, J. E. dos Santos, G. L. M. P. Rodrigues, A. S. Rocha, H. R. de Moraes, and J. C. Cezar, "Ultrahigh-vacuum organic molecular-beam deposition system for *in situ* growth and characterization," J. Synchrotron Radiat. **25**, 1658 (2018).

[41] C. Nicklin, J. Martinez-Hardigree, A. Warne, S. Green, M. Burt, J. Naylor, A. Dorman, D. Wicks, S. Din, and M. Riede, "MINERVA: A facility to study Microstructure and INterface Evolution in Realtime under VAcuum," Rev. Sci. Instrum. **88**, 103901 (2017).

[42] P. Krasuski, "Angular distribution of flux at the exit of cylindrical tubes," J. Vac. Sci. Technol., A **5**, 2488 (1987).

[43] R. Ruiz, D. Choudhary, B. Nickel, T. Toccoli, K.-C. Chang, A. C. Mayer, P. Clancy, J. M. Blakely, R. L. Headrick, S. Iannotta, and G. G. Malliaras, "Pentacene thin film growth," Chem. Mater. **16**, 4497 (2004).

[44] A. Aufderheide, K. Broch, J. Novák, A. Hinderhofer, R. Nervo, A. Gerlach, R. Banerjee, and F. Schreiber, "Mixing-induced anisotropic correlations in molecular crystalline systems," Phys. Rev. Lett. **109**, 156102 (2012).

[45] A. Hinderhofer and F. Schreiber, "Organic–organic heterostructures: Concepts and applications," ChemPhysChem **13**, 628 (2012).

[46] A. R. J. Nelson and S. W. Prescott, "refnx: Neutron and X-ray reflectometry analysis in Python," J. Appl. Crystallogr. **52**, 193 (2019).

[47] S. Kowarik, A. Gerlach, and F. Schreiber, "Organic molecular beam deposition: Fundamentals, growth dynamics, and *in situ* studies," J. Phys.: Condens. Matter **20**, 184005 (2008).

[48] H. Zhu, Q. L. Li, X. J. She, and S. D. Wang, "Surface roughening evolution in pentacene thin film growth," Appl. Phys. Lett. **98**, 243304 (2011).

[49] A. C. Dürr, F. Schreiber, M. Münch, N. Karl, B. Krause, V. Kruppa, and H. Dosch, "High structural order in thin films of the organic semiconductor diindenoperylene," Appl. Phys. Lett. **81**, 2276 (2002).

[50] A. Hinderhofer, J. Hagenlocher, A. Gerlach, J. Krug, M. Oettel, and F. Schreiber, "Nonequilibrium roughness evolution of small molecule mixed films reflecting equilibrium phase behavior," J. Phys. Chem. C **126**, 11348 (2022).

[51] F. Unger, D. Lepple, M. Asbach, L. Craciunescu, C. Zeiser, A. F. Kandolf, Z. Fišer, J. Hagara, J. Hagenlocher, S. Hiller *et al.*, "Optical absorption properties in pentacene/tetracene solid solutions," J. Phys. Chem. A **128**, 747 (2024).

[52] A. R. Denton and N. W. Ashcroft, "Vegard's law," Phys. Rev. A **43**, 3161 (1991).